Atmos. Chem. Phys. Discuss., https://doi.org/10.5194/acp-2019-302
Manuscript under review for journal Atmos. Chem. Phys.
Discussion started: 29 April 2019

Atmospheric Chemistry and Physics
Discussions

Impact of convectively lofted ice on the seasonal cycle of tropical lower stratospheric water vapor

Xun Wang[1], Andrew E. Dessler[1], Mark R. Schoeberl[2], Wandi Yu[1], and Tao Wang[3]

[1]Department of Atmospheric Sciences, Texas A&M University, College Station, TX, USA
[2]Science and Technology Corporation, Columbia, MD, USA
[3]University of Maryland, College Park, MD, USA

Correspondence to: Andrew E. Dessler (adessler@tamu.edu)

Abstract. We use a forward Lagrangian trajectory model to diagnose mechanisms that produce the tropical lower stratospheric (LS) water vapor seasonal cycle observed by the Microwave Limb Sounder (MLS) and reproduced by the Goddard Earth Observing System Chemistry Climate Model (GEOSCCM) in the tropical tropopause layer (TTL). We confirm in both the MLS and GEOSCCM that the seasonal cycle of water vapor is primarily determined by the seasonal cycle of TTL temperatures. However, we find that the seasonal cycle of temperature predicts a smaller seasonal cycle of LS water vapor between 10°N-40°N than observed by MLS. We show that including evaporation of convectively lofted ice in the trajectory model increases the simulated maximum value in the 10°N-40°N water vapor seasonal cycle by 1.9 ppmv (47%) and increases the seasonal amplitude by 1.26 ppmv (123%), which improves the prediction of LS water vapor annual cycle. We conclude that the moistening effect from convective ice evaporation in the TTL plays a key role regulating and maintaining the tropical LS water vapor seasonal cycle. Most of the convective moistening in the 10°N-40°N range comes from convective ice evaporation occurring at the same latitudes. A small contribution to the moistening comes from convective ice evaporation occurring between 10°S-10°N. Within 10°N-40°N, the Asian monsoon region is the most important region for convective ice evaporation and convective moistening during boreal summer and autumn.

1 Introduction

Stratospheric water vapor is important for the radiative budget of the atmosphere and the regulation of stratospheric ozone (e.g. Solomon et al., 1986; Dvortsov and Solomon, 2001). One of the key features of the tropical lower stratospheric (LS) water vapor is its seasonal cycle often referred to as the "tape recorder" (e.g. Mote et al., 1995, 1996). The amount of water vapor entering the stratosphere and its seasonal cycle is primarily controlled by temperatures in the tropical tropopause layer (TTL) (e.g. Brewer, 1949; Holton et al., 1995; Fueglistaler et al., 2009). The low TTL temperatures freeze-dry the air, reduce the water vapor mixing ratio to local saturation, and imprint the seasonal cycle on air ascending into the stratosphere (e.g. Mote et al., 1996; Fueglistaler, 2005; Schoeberl et al., 2008; Fueglistaler et al., 2009).

Analyses of observations have suggested that deep convection reaching the TTL is also important for regulating the amount of water vapor entering the stratosphere. Nielsen et al. (2007) and Corti et al. (2008) suggested that deep penetrating convection deposits ice particles above the cold point tropopause, where ice may evaporate and cause a moistening effect. This idea is also supported by observations of enrichment of the deuterated isotopologue of water vapor (HDO) in the tropical LS, which suggests moistening by evaporated convective cloud ice (Moyer et al., 1996; Dessler et al., 2007; Steinwagner et al., 2010). The role of convective ice evaporation in the stratospheric entry water vapor has also been addressed in several model studies. Dessler and Sherwood (2004) used simple budget models with and without convection and concluded that, during summer, moistening by deep penetrating convection increases the northern hemisphere extratropical water vapor at 380-K isentrope by 40%. Ueyama et al. (2015) included convective ice evaporation in the trajectory model simulation with observed convective cloud top and concluded that convection moistens the 100 hPa level by 0.3 ppmv in boreal winter (which is less than 10%). Schoeberl et al. (2014, 2018) quantified the global impact of convective ice on winter 2008/2009 water vapor between 18-30 km, and concluded that, for global average water vapor between 18-30 km during winter, the convective ice evaporation plays only a small role, since convection rarely reach the level of the tropopause cold point. They suggested that warmer temperatures or higher penetrating convection may result in more hydration from the convection ice evaporation. During El Niño events, convective ice evaporation appears to play a larger role in the interannual variability of water vapor entering the stratosphere (Avery et al., 2017; Ye et al., 2018). On longer time scales, convective ice evaporation is found to contribute to an important fraction of the increase of LS water vapor over the next century in two chemistry-climate models (Dessler et al., 2016).

The goal of this paper is to investigate the impact of convective ice on the seasonal cycle of water vapor in the TTL and LS. Previous analyses have focused on global impact, interannual variability, and the longterm trend (e.g. Ueyama et al., 2015; Dessler et al., 2016; Avery et al., 2017; Schoeberl et al., 2014, 2018; Ye et al., 2018). However, there is a strong seasonal cycle in LS water vapor and less work has been done on understanding the impact of convective ice. The basics of the water vapor seasonal cycle can be understood simply: more water vapor enters the LS during boreal summer, when TTL temperatures are generally higher and vice versa during boreal winter. But closer examination of the data reveals some deficiencies in this simple picture. Figures 1b-c show the MLS seasonal cycle of water vapor. At 100 hPa and 82.5 hPa, the zonal mean water vapor is observed to have maximum seasonal oscillation in the northern hemispheric subtropics (e.g. Rosenlof, 1997; Randel et al., 1998, 2001, and references therein) despite the fact that the temperature seasonal cycle is symmetric about the equator (Figs. 1b-c). As water vapor is transported further upward, the hemispheric asymmetry feature in the seasonal cycle gradually disappears (Fig. 1a) (e.g. Randel et al., 1998, 2001). The lower altitude hemispheric asymmetry indicates that processes other than dehydration by large-scale TTL temperatures may play a role in the LS water vapor budget.

Previous studies have suggested that this hemispheric asymmetry structure in the water vapor seasonal cycle is due to processes within the Southeast Asian monsoon and North American monsoon region, including both diabatic and adiabatic

Atmos. Chem. Phys. Discuss., https://doi.org/10.5194/acp-2019-302
Manuscript under review for journal Atmos. Chem. Phys.
Discussion started: 29 April 2019

transport in the TTL and lowermost stratosphere (e.g. Rosenlof, 1997; Randel et al., 1998; Dethof et al., 1999; Bannister et al., 2004; Gettelman et al., 2004; Pan et al., 1997, 2000, Park et al., 2004, 2007; Wright et al., 2011; Ploeger et al., 2013). Indeed, the MLS data (Fig. 2c) show that the summertime maxima of the LS water vapor is confined in the Asian monsoon and North American monsoon anti-cyclone at 100 hPa (e.g. Rosenlof, 1997; Jackson et al., 1998; Randel et al., 1998, 2001; Dessler and Sherwood, 2004; Randel and Park, 2006; Park et al., 2007; Bian et al., 2012) and become weaker above 100 hPa (Figs. 2a-b).

Other studies have investigated impact of convectively injected water vapor and overshooting deep convection within the monsoon regions on the budget of the topical LS water vapor. Fu et al. (2006) suggested that the deep convection over the Tibetan Plateau acts as a short circuit of water vapor ascending across the tropical tropopause. James et al. (2008), using a trajectory model, suggested that air parcels are lifted by convection over Southeast Asia and then transported into the TTL by the monsoon anticyclone, avoiding the cold pool in the deep tropics. However, they pointed out that direct convective injection has a limited impact on the water vapor budget, contributing to 0.3 ppmv of the water vapor in the Asian monsoon region. Schwartz et al. (2013) provided evidence of occasional enhanced lowermost stratospheric water vapor by convective injection over the Asian and North American monsoon regions using satellite observations. Randel et al. (2015) investigated subseasonal variations in LS water vapor in the northern hemisphere monsoon regions and suggested that stronger convection leads to lower TTL temperatures in the monsoon regions, which results in less LS water vapor there, thereby concluding that the LS water vapor in the monsoon regions is mainly controlled by large-scale transport and TTL temperatures there.

The role of convective ice evaporation in the tropical LS water vapor seasonal cycle, however, has not been fully explored. The seasonal cycle is one of the key features of the tropical LS water vapor, so it is important that we fully understand the mechanisms that drive it. In this study, we quantitatively test whether moistening by convective ice evaporation is playing a role in the tropical LS water vapor seasonal cycle.

2 Models and Data

2.1 MLS water vapor

We analyse here version 4.2 level 2 water vapor retrieved from the Earth Observing System (EOS) Microwave Limb Sounder (MLS) instrument on the Aura spacecraft (Livesey et al., 2017). Since August 2004, the MLS provides ~3500 vertical scans of the earth's limb from the surface to 90 km each day, covering a latitude range of 82°S to 82°N with a horizontal resolution of 1.5°along the orbit track (Lambert et al., 2007). The MLS water vapor retrieval has a vertical resolution of about 3 km in the TTL, with precision at 100 hPa and 82.5 hPa of 15% and 7%, respectively. The accuracy of the water vapor at 100 hPa and 82.5 hPa is 8% and 9%, respectively (Livesey et al., 2017). We composite the daily standard water vapor between August 2004 to October 2018 to produce monthly mean averaged on a horizontal grid of 4°latitude by 8°longitude following the data-screening in Livesey et al., (2017).

2.2 Ice Water Content from Cloud-Aerosol Lidar with Orthogonal Polarization

The Cloud-Aerosol Lidar with Orthogonal Polarization (CALIOP) is a two-wavelength polarization elastic backscatter lidar that detects global tropospheric and lower stratospheric aerosol and cloud profiles (Hu et al., 2009; Liu et al., 2009; Vaughan et al., 2009; Winker et al., 2009, 2010; Young and Vaughan, 2009; Avery et al., 2012; Heymsfield et al., 2014). We use the CALIOP Level 2 Cloud Profile Product in version 4.2, with horizontal resolution of 5 km along-track and 60 m vertically in the TTL and LS. The CALIOP cloud Ice Water Content (IWC) is derived from a parameterized function of the CALIOP 532 nm cloud particle extinction profiles (Avery et al., 2012; Heymsfield et al., 2014). We use IWC from all ice clouds detected by the CALIOP, since the CALIOP does not separate convective from non-convective IWC measurements. In this study, we average and interpolate the CALIOP IWC into monthly gridded fields on pressure levels using data from 2007 to 2017.

2.3 GEOSCCM

We also analyze simulations of the TTL and LS from the Goddard Earth Observing System Chemistry Climate Model (GEOSCCM). The GEOSCCM couples the GEOS-5 general circulation model (Rienecker et al., 2008; Molod et al., 2012) to a comprehensive stratospheric chemistry module (Oman and Douglass, 2014; Pawson et al., 2008). The run analysed here starts in 1998 and ends in 2099 and driven by the Representative Concentration Pathway (RCP) 6.0 greenhouse gas scenario (Van Vuuren et al., 2011) and the A1 scenario for ozone depleting substances (World Meteorological Organization, 2011). Sea surface temperatures and sea ice concentrations were prescribed from Community Earth System Model version 1 simulations (Gent et al., 2011). The model has a horizontal resolution of 2°latitude by 2.5°longitude and 72 vertical levels up to the model top at 0.01 hPa (Molod et al., 2012). The GEOSCCM uses a single moment cloud microphysics scheme (Bacmeister et al., 2006; Barahona et al., 2014). The convective IWC in the GEOSCCM originates in moist detraining convection, which uses Relaxed Arakawa-Schubert convective parameterization (Moorthi and Suarez, 1992).

2.4 Trajectory Model

In this study, we use the forward, domain filling, diabatic trajectory model described in Schoeberl and Dessler (2011) and updated in subsequent publications. The trajectory model uses 6-hourly instantaneous horizontal winds and 6-hourly average diabatic heating rates to advect parcels using the Bowman trajectory code (Bowman, 1993; Bowman and Carrie, 2002), from a variety of sources such as the European Centre for Medium-Range Weather Forecasts (ECMWF) ERA-interim (ERAi), and Modern-Era Retrospective analysis for Research and Applications-2 (MERRA-2) (Molod et al., 2015; Gelaro et al., 2017), and the GEOSCCM.

Atmos. Chem. Phys. Discuss., https://doi.org/10.5194/acp-2019-302
Manuscript under review for journal Atmos. Chem. Phys.
Discussion started: 29 April 2019

In this study, the trajectory model initializes 1350 dimensionless parcels daily in the upper troposphere on an equal area longitude-latitude grid covering 0-360°longitude and ± 60°latitude, and with initial water vapor mixing ratio of 200 parts per million by volume (ppmv). The initialization level is at 370 K potential temperature, which is above the average level of zero heating (~355-360 K) (Fueglistaler et al., 2009) but below the tropical tropopause (~380 K). At the end of each day, parcels below the 250-hPa pressure surface or above the 5000-K isentrope are removed because they are considered outside of the model boundaries.

Along each trajectory, an instant dehydration scheme is used. In this scheme, anytime the RH (with respect to ice) exceeds the dehydration threshold, water vapor is instantly removed to reduce RH to the dehydration threshold. The pre-set dehydration threshold is 100% RH for the ERAi trajectory runs and MERRA-2 trajectory runs. For the GEOSCCM trajectory runs, the pre-set dehydration threshold is 80% RH, since in the GEOSCCM dehydration occurs when the grid-average RH is around this value (Molod et al., 2012). The same parameterization for the pre-set RH threshold of 80% was used successfully to analyse the GEOSCCM in Dessler et al. (2016) and Ye et al. (2018), which produces water vapor in good agreement with the observations. In all trajectory runs, the parcel temperature is calculated by linearly interpolating 6-hourly temperatures in time and space to parcel locations at each time step; the RH is computed using the saturation mixing ratio at that temperature (Murphy and Koop, 2005). The trajectory model includes methane oxidation as a water source as described in Schoeberl and Dessler (2011), but this process is unimportant in the TTL and LS. We will refer to this version as the "standard" trajectory model – another version that includes ice evaporation will be introduced later.

As an alternative to instant dehydration we can use a cloud model, which is described in Schoeberl et al. (2014). The cloud model triggers ice nucleation at a prescribed nucleation RH (NRH) threshold and the number of ice particles produced upon nucleation is proportional to the parcel cooling rate using the relationship derived by Kärcher et al. (2006). The ice mixing ratio is carried with the parcel along with number of crystals and size. Ice crystal distribution has a single size mode that varies as the parcels grow or sublimate. Gravitational sedimentation reduces the total ice amount within the parcel. Ice crystals are assumed to be spheres which is reasonable for small crystals in the upper troposphere (Woods et al., 2018). The cloud model uses a fixed cloud geometrical thickness of 500 m based on the TTL cloud thickness distribution observed by CALIOP (Schoeberl et al., 2014). We also assume that ice falling out of the cloud slowly sublimates in sub-saturated layers well below the cloud. The cloud model produces good agreement with observational data from aircraft flights (Schoeberl et al., 2015). The cloud model incorporates more realistic physics than the instant dehydration scheme we use in the standard trajectory model. The physics in the cloud model has a net effect of slowing down the parcels' dehydration rate and increasing water vapor in the LS compared to the instant dehydration scheme (Schoeberl et al., 2014).

We start all trajectory models on 1/1/2000 and analyze the model results from 2005 to October 2018, so that we can compare the ERAi and MERRA-2 driven trajectory results to the MLS observations. The GEOSCCM is a free-running model, so

Atmos. Chem. Phys. Discuss., https://doi.org/10.5194/acp-2019-302
Manuscript under review for journal Atmos. Chem. Phys.
Discussion started: 29 April 2019

interannual variability of the model will not match MLS observations. We will therefore compare the average results from the GEOSCCM to observations.

3 Results

3.1 Impact of convective moistening on the seasonal cycle

Figures 1d-i show the water vapor seasonal cycle at 100 hPa, 82.5 hPa, and 68 hPa simulated by the standard trajectory model driven by ERAi, and MERRA-2 in which dehydration is entirely driven by temperature and there is no convective influence (See Table 1 for summary of the trajectory model cases). To compare with the MLS, we averaged the trajectory water vapor fields in the vertical using the MLS averaging kernels following the instructions from Livesey et al. (2017). Unlike the MLS observations, the trajectory models fail to produce the larger maximum water vapor values in the northern hemisphere subtropics in August-September at 100 hPa and 82.5 hPa (Figs. 1e-f and 1h-i). At 68 hPa, the trajectory models agree with the MLS that the seasonal cycle is approximately centered over the equator, although it underpredicts the MLS (Figs. 1a, 1d, and 1g). During June-July-August (JJA) (Figs. 2d-i), the trajectory models underestimate the maxima over the Asian and North American monsoon regions (Figs. 2e, 2f, 2h, and 2i). At 68 hPa, the monsoonal maxima are nearly gone and the trajectory models do a reasonable job of simulating the spatial patterns (Figs. 2d and 2g).

We also ran the ERAi and MERRA-2 simulation with the cloud model described in Section 2.4 operating along the trajectory model, with 100% NRH (Table 1). Note that this version of the trajectory model does not have any convective ice in it, so water vapor is still regulated entirely by TTL temperatures. Figures 1j-o show that the cloud model produces larger water vapor values in the seasonal cycles at 100 hPa, 82.5 hPa, and 68 hPa. However, the cloud model doesn't help reproduce the hemispheric asymmetry feature in the seasonal cycles at 100 hPa and 82.5 hPa – it basically increases water vapor both north and south of the equator. During JJA (Figs. 2l and 2o), the cloud model helps reproduce the 100-hPa water vapor maxima over the Asian monsoon and North American monsoon regions, but it results in overestimated water vapor values over the Southern hemispheric subtropics. Thus, regardless of dehydration scheme, models that regulate water vapor only through TTL temperatures and large-scale transport do not reproduce important features of the TTL/LS water vapor seasonal cycle, including the observed hemispheric asymmetry.

Our hypothesis is that convective moistening is causing the hemispheric asymmetry in the water vapor seasonal cycle. To test this idea, we perform a parallel analysis with the GEOSCCM, a model where evaporation of convective ice is known to add water to the TTL (Dessler et al., 2016; Ye et al., 2018). In our experiment, we first run the standard trajectory model driven by meteorology from the GEOSCCM which, like the standard models analysed above, uses instant dehydration to regulate water vapor exclusively through TTL temperatures. We also run a second version of the trajectory model, the "ice model", in which we add the evaporation of convectively lofted ice to the trajectory model. To do that, we linearly interpolate the GEOSCCMs' 6-hourly three-dimensional convective IWC field to the location and time of each trajectory's time step. Then, at each time step, we assume complete evaporation of this ice into the parcel by adding the GEOSCCM convective IWC to the parcel's water vapor — although we do not let parcels exceed the pre-set RH threshold of 80%. Since we assume instant evaporation of the ice, we consider this to be an upper limit of the impact of convective ice evaporation on the water content of the TTL and LS (Dessler et al., 2016).

In Figures 3 and 4, we compare GEOSCCM convective IWC with CALIOP IWC. Note the CALIOP data includes all IWC, both convective and in situ, while GEOSCCM fields are for convection only. There's general agreement between GEOSCCM convective IWC and CALIOP IWC, which sets the groundwork for our convective moistening scheme. One clear difference is that the GEOSCCM convective IWC fields cover a narrower latitude range than the CALIOP IWC (Fig. 3) – in particular, there is a tail of IWC in the CALIOP data in the DJF mid-latitudes that is missing in the GEOSCCM. Additionally, the GEOSCCM tends to have higher amounts of ice at each altitude level below about 100 hPa. The spatial pattern of CALIOP IWC (Fig. 4) is well reproduced by the GEOSCCM convective IWC, although the GEOSCCM generally has smaller values as expected since stratiform clouds aren't included in the GEOSCCM convective IWC.

The water vapor seasonal cycles from the GEOSCCM and various GEOSCCM trajectory model runs (Table 1) are shown in Fig. 5. These have also been re-averaged in the vertical using the MLS averaging kernels (Livesey et al., 2017) to facilitate comparison with MLS. We focus on the 100-hPa level, where the hemispheric asymmetry is strongest. The GEOSCCM agrees with the MLS (Fig. 1c) that the 100-hPa water vapor has a larger seasonal oscillation over 10°N-40°N than 10°S-40°S, and that during JJA the 100-hPa water vapor maxima are located over the Asian monsoon and North American monsoon regions (Figs. 5a-b). The standard trajectory model, which regulates water entirely through TTL temperatures, underestimates the maximum values and amplitude of the GEOSCCM seasonal cycle in the northern hemispheric subtropics by 1.3 ppmv (24%) and 1.15 ppmv (52%), respectively. It also underestimates the JJA water vapor values in the Asian monsoon region and North American monsoon region (Figs. 5c-d). These results are similar to the comparison between MLS and the standard trajectory models driven by ERAi and MERRA-2 (Fig. 1f and 1i). The ice model, which includes evaporation of convective ice, shows a clear hemispheric asymmetry in the LS water vapor seasonal cycle and more pronounced seasonal maxima over the monsoon regions (Figs. 5e and 5f). Specifically, compared to the standard model, evaporation of convectively lofted ice increases the maximum value of the 10°N-40°N water vapor seasonal cycle by 1.9 ppmv (47%) in September.

These results suggest that convective ice evaporation is important to the water vapor seasonal cycle in the northern hemispheric subtropics in the GEOSCCM. Dessler et al. (2016) analysed this same GEOSCCM run and showed that ice evaporation is required to accurately simulate the long-term trend in stratospheric water vapor. Our results are also similar to that obtained by Ye et al. (2018), who also analysed this GEOSCCM and showed that ice evaporation is required to reproduce the model's interannual variability of tropical LS water vapor. They found that the observed convective cloud occurrence frequency in the TTL increases as the troposphere warms, and that the GEOSCCM produces a similar correlation between the convective cloud IWC and tropospheric temperature. This helped explain the moistening effect from the increased convective cloud ice, which contributes to an important part of the tropical LS water vapor interannual variability in both the observations and the GEOSCCM as the troposphere warms. This also demonstrated a consistency between the GEOSCCM and the observations, which provides confidence that the behaviour of the GEOSCCM is realistic.

Fig. 6 shows the 100-hPa water vapor seasonal cycles in the northern hemispheric subtropics (10°N-40°N), deep tropics (10°S-10°N), and southern hemispheric subtropics (10°S-40°S). To aid in comparison, we have subtracted the annual mean from each data set. The standard model generally agrees well with the GEOSCCM and MLS in the 10°S-10°N and 10°S-40°S region (Figs. 6b-d). This suggests that the water vapor seasonal cycle in those regions is mainly controlled by the TTL temperatures and large-scale transport and implying that other factors, including convective ice evaporation, are less important. In the 10°N-40°N region, however, the standard model does a poor job, predicting an amplitude that is about half the amplitude of the GEOSCCM and MLS (Figures. 6a and 6d). The ice model, however, produces boreal summer and autumn water vapor values in the 10°N-40°N much closer to the GEOSCCM and MLS; it increases the 10°N-40°N seasonal amplitude by 1.26 ppmv (123%). This means convective ice evaporation is particularly important to the maximum water vapor value in northern hemispheric subtropics during boreal summer and autumn, thereby playing a key role in the seasonal cycle there.

We note that the ice model does a good job reproducing the seasonal variations in the 10°N-40°N region (Fig. 6), but the absolute water vapor values it produced are generally overestimated compared to the GEOSCCM and MLS (Fig. 5). This is likely because the convective moistening scheme we used in the trajectory model instantly evaporates convective ice and hydrates parcels to the saturation threshold. We did another GEOSCCM trajectory analysis, in which we specify that evaporation relaxes the RH towards 80% with an e-folding time scale τ of 6 hours. Figures 5g-h show that this finite time ice evaporation scheme helps reduce the overestimation and produces water vapor values closer to the GEOSCCM. This reinforces the idea that the ice model we use in this paper provides an upper limit of the impact of convective ice evaporation on the water content of the TTL and LS (Dessler et al., 2016).

3.2 Source regions of convective ice evaporation

Our results suggest that convective ice evaporation contributes an important part of the water vapor seasonal cycle in the 10°N-40°N region. This then begs the question of which region contributes most to this convective moistening? Here we define the quantity net convective moistening to be the water vapor mixing ratio in the ice model minus that in the standard trajectory model. The net convective moistening thus represents the net water vapor added by convective ice evaporation. We also quantify the rate of convective ice evaporation in the ice model. To do this, we record the location and amount of water vapor added to each parcel from ice evaporation on every time step. We then grid and average these values to produce a three-dimensional field of the ice evaporation rate (in units of ppmv day^{-1}). Note that water vapor added by convection will not necessarily make it into the stratosphere — the added water vapor may be removed in subsequent dehydration events.

Fig. 7a shows that from January to May, the convective IWC is abundant in the deep tropics between 20°S-20°N, but it doesn't produce large ice evaporation rates (Fig. 7b) or large net convective moistening (Fig. 7d). This is a consequence of high RH during this period (Fig. 7c), which suppresses evaporation of convectively lofted ice. From June to September, on the other hand, RH is lower, so while there is less ice lofted in the TTL, it efficiently evaporates. This can be seen in Figs. 7b and 7d, which show maximum ice evaporation rates and net convective moistening during this time, located between 10°S-40°N, where the convective IWC is abundant. Between 10°S-40°S, however, there is little convective IWC available even though the RH is low, resulting in small evaporation rates and net convective moistening. Thus, the ice evaporation rate and net convective moistening are due to a combination of available convective IWC abundance and RH below saturation (Dessler and Sherwood, 2004).

Both the ice evaporation rate and net convective moistening during June to September has maximum values between 10°N-40°N, which suggests that net convective moistening in the 10°N-40°N water vapor seasonal cycle is largely contributed by local convective ice evaporation. But there is also a large evaporation rate between 10°S-10°N (Fig. 7b). To determine if this tropical evaporation is contributing to the 10°N-40°N seasonal cycle, we separately track the amount of water vapor in the 10°N-40°N region that is produced by evaporation of convective ice (net convective moistening) between 10°N-40°N and 10°S-10°N. Fig. 8 shows the seasonal cycle of net convective moistening at 100 hPa in the 10°N-40°N region contributed by evaporation of convective ice between 10°N-40°N and 10°S-10°N. We note that to obtain the absolute values of net convective moistening, we do not subtract annual mean from the seasonal cycles like we did in Fig. 6. During the winter (DJF), contributions from ice evaporation between 10°S-10°N and 10°N-40°N are about even, but during the summertime (JJA), evaporation of convective ice in the 10°N-40°N region is the dominant contributor to the net convective moistening. Specifically, it contributes to 1.46 ppmv (71%) and 1.09 ppmv (86%) of the net convective moistening in the 10°N-40°N water vapor seasonal maximum (September) value and seasonal amplitude. Convective ice evaporation between 10°S-10°N plays a smaller role, contributing to 0.50 ppmv (24.7%) and 0.12 ppmv (9.9%) of the net convective moistening in the 10°N-40°N water vapor seasonal maximum value and seasonal amplitude.

Next, we investigate net convective moistening in the 10°N-40°N water vapor seasonal cycle contributed by specific regions within the 10°S-40°N domain. To do this, we divide the 10°S-40°N domain into 12 equal-area boxes. We calculate the net convective moistening contributed by each of these boxes using the same method we used to calculate the contribution by 10°N-40°N and 10°S-10°N. Fig. 9 shows the contribution from each box region to the net convective moistening in the 10°N-40°N water vapor seasonal maximum value in September and the seasonal amplitude.

We find that contribution from the box regions over Southeast Asia (10°N-40°N, 60°E-120°E), subtropical Western Pacific (10°N-40°N, 120°E-180°E), and North America (10°N-40°N, 120°W-60°W) dominate. The Southeast Asia region contributes to 0.56 ppmv (27%) and 0.37 ppmv (30%) of the net convective moistening in the 10°N-40°N water vapor seasonal maximum value and seasonal amplitude. The subtropical Western Pacific also contributes to the net convective moistening in the 10°N-40°N water vapor seasonal cycle. This is due to the abundant convective IWC over the subtropical west Pacific (Fig. 4b), which is likely related to the east-west oscillation of the Asian monsoon anticyclone (Pan et al., 2016; Luo et al., 2018). The North America region is less important, contributing to 0.25 ppmv (12%) and 0.15 ppmv (12%) of the net convective moistening in the 10°N-40°N water vapor seasonal maximum value and seasonal amplitude. This is because most of the convective IWC in the GEOSCCM over the North American monsoon region is found below 100 hPa (not shown).

4 Conclusion

In this study, we investigate mechanisms that drive the seasonal cycle of TTL and tropical lower stratospheric (LS) water vapor. We use a Lagrangian trajectory model (Schoeberl and Dessler, 2011) to analyse the seasonal cycle in observations of water vapor made by the Microwave Limb Sounder (MLS) (Lambert et al., 2007; Livesey et al., 2017) as well as simulated fields from the Goddard Earth Observing System Chemistry Climate Model (GEOSCCM) (Rienecker et al., 2008; Molod et al., 2012; Pawson et al., 2008; Oman and Douglass, 2014).

Water vapor's seasonal cycle in the tropical LS, sometimes referred to as the "tape recorder," has highest values of water vapor entering the stratosphere during Northern Hemispheric summer. We confirm in both the MLS observations and in the GEOSCCM that this is mainly due to the seasonal cycle of TTL temperatures. However, closer examination of the data reveals some deficiencies in this simple picture. Both the MLS and GEOSCCM show that the tropical LS water vapor seasonal cycle has a hemispheric asymmetry, with maximum seasonal cycle between 10°N-40°N near the tropopause level, despite the fact that the TTL temperature seasonal cycle is symmetric about the equator (e.g. Rosenlof, 1997; Randel et al., 1998, 2001, and references therein). Trajectory models that only regulate TTL water vapor using temperatures (Schoeberl and Dessler, 2011) from reanalysis and GEOSCCM all produce weaker water vapor seasonal cycles between 10°N-40°N compared to the MLS and GEOSCCM. These indicate that the seasonal oscillation between 10°N-40°N is too large to be simply explained by TTL temperatures.

Recent studies suggested that evaporation of convectively injected ice in the TTL also contributes to the amount of water vapor entering the stratosphere (Nielsen et al., 2007; Corti et al., 2008; Steinwagner et al., 2010; Ueyama et al., 2015; Dessler et al., 2016; Schoeberl et al., 2014, 2018; Ye et al., 2018). To better understand this, we analyse a chemistry-climate model where evaporation of convective ice is known to add water to the TTL (Dessler et al., 2016; Ye et al., 2018). Previous work (Ye et al., 2018) has shown that the behaviour of the LS water vapor and convection in the GEOSCCM are reasonable and agree well with observations. We extend that here by showing that there is general agreement between GEOSCCM convective ice water content (IWC) and IWC from Cloud-Aerosol Lidar with Orthogonal Polarization (CALIOP) observations (Hu et al., 2009; Liu et al., 2009; Vaughan et al., 2009; Winker et al., 2009, 2010; Young and Vaughan, 2009; Avery et al., 2012; Heymsfield et al., 2014).

Using a version of the trajectory model driven by GEOSCCM meteorology that includes evaporation of convectively lofted ice, we obtained a more accurately simulated seasonal cycle of the LS water vapor between 10°N-40°N and the hemispheric asymmetry compared to the GEOSCCM. Convective ice evaporation in this ice model increases the maximum value of the 10°N-40°N water vapor seasonal cycle by 1.9 ppmv (47%) and increases the 10°N-40°N seasonal amplitude by 1.26 ppmv (123%) compared to standard model.

A major part of the convective moistening in the 10°N-40°N water vapor seasonal cycle is contributed by convective ice evaporation in the 10°N-40°N latitudinal range during boreal summer. The maximum convective ice evaporation in this region is due to available convective IWC and relative humidity low enough to allow it to evaporate (Dessler and Sherwood, 2004). Ice evaporation between 10°N-40°N contributes to 1.46 ppmv (71%) and 1.09 ppmv (86%) of the net convective moistening in the 10°N-40°N water vapor seasonal maximum value and seasonal amplitude. Between 10°N-40°N, the Asian monsoon region is the most important region for convective ice evaporation and convective moistening. Convective ice evaporation in other regions, including the deep tropics between 10°S-10°N, has a smaller influence in LS water vapor between 10°N-40°N.

To summarize, we find that TTL temperature variations alone cannot explain the seasonal cycle of water vapor in MLS observations of the TTL over the northern hemisphere subtropics, 10°N-40°N (although temperature does explain the seasonal cycle it the tropics, 10°S-10°N and southern subtropics, 10°S-40°S). To try to understand the other mechanisms at work, we analyse a climate model, the GEOSCCM, which reproduces the MLS observations and has been shown to accurately simulate the TTL. We find that evaporation of convective ice is responsible for the large seasonal cycle in the GEOSCCM in the northern hemisphere subtropics. We therefore conclude that evaporation of convective ice, mainly in boreal summer, is the most likely explanation for the large seasonal cycle in the northern hemisphere subtropics. We concur that the seasonal cycle of the TTL temperatures is the major driver of the seasonal cycle of tropical LS water vapor, but we find that the contribution from evaporation of convective ice fill in more details of this simple picture. Our findings emphasize the need to better understand and quantify the magnitude and spatial pattern of convective ice evaporation in the TTL.

Data availability. The water vapor observed by MLS is available from https://mls.jpl.nasa.gov/. The ice water content observed by CALIOP is available from https://eosweb.larc.nasa.gov/. The MERRA-2 meteorological fields are available

Atmos. Chem. Phys. Discuss., https://doi.org/10.5194/acp-2019-302
Manuscript under review for journal Atmos. Chem. Phys.
Discussion started: 29 April 2019

from https://disc.gsfc.nasa.gov/. The ERAi meteorological fields are available from https://www.ecmwf.int/en/forecasts/datasets/reanalysis-datasets/era-interim.

Competing interests. The authors declare that they have no conflict of interest.

Author contribution. Xun Wang performed analysis, and wrote the original draft. Andrew E. Dessler provided the conceptualization, guidance, and editing. Mark R. Schoeberl and Tao Wang contributed to the trajectory model code, methodology, discussion, and editing. Wandi Yu contributed to methodology and discussion.

Acknowledgments. This work was supported by NASA grants NNX16AM15G and 80NSSC18K0134, both to Texas A&M University. We would like to thank Dr. Luke Oman for providing the GEOSCCM meteorological fields used in this study.

References

Avery, M., Winker, D., Heymsfield, A., Vaughan, M., Young, S., Hu, Y. and Trepte, C.: Cloud ice water content retrieved from the CALIOP space-based lidar, Geophys. Res. Lett., 39(5), n/a-n/a, doi:10.1029/2011gl050545, 2012.
Avery, M. A., Davis, S. M., Rosenlof, K. H., Ye, H. and Dessler, A. E.: Large anomalies in lower stratospheric water vapour and ice during the 2015–2016 El Niño, Nat. Geosci., 10(6), 405–409, doi:10.1038/ngeo2961, 2017.
Bacmeister, J. T., Suarez, M. J. and Robertson, F. R.: Rain Reevaporation, Boundary Layer–Convection Interactions, and Pacific Rainfall Patterns in an AGCM, J. Atmos. Sci., 63(12), 3383–3403, doi:10.1175/JAS3791.1, 2006.
Bannister, R. N., O'Neill, A., Gregory, A. R. and Nissen, K. M.: The role of the south-east Asian monsoon and other seasonal features in creating the 'tape-recorder' signal in the Unified Model, Q. J. R. Meteorol. Soc., 130(599), 1531–1554, doi:10.1256/qj.03.106, 2004.
Barahona, D., Molod, A., Bacmeister, J., Nenes, A., Gettelman, A., Morrison, H., Phillips, V. and Eichmann, A.: Development of two-moment cloud microphysics for liquid and ice within the NASA Goddard Earth Observing System Model (GEOS-5), Geosci. Model Dev., 7(4), 1733–1766, doi:10.5194/gmd-7-1733-2014, 2014.
Bian, J., Pan, L. L., Paulik, L., Vömel, H., Chen, H. and Lu, D.: In situ water vapor and ozone measurements in Lhasa and Kunming during the Asian summer monsoon, Geophys. Res. Lett., 39(19), n/a-n/a, doi:10.1029/2012GL052996, 2012.
Bowman, K. P.: Large-scale isentropic mixing properties of the Antarctic polar vortex from analyzed winds, J. Geophys. Res. Atmos., 98(D12), 23013–23027, doi:10.1029/93JD02599, 1993.
Bowman, K. P. and Carrie, G. D.: The mean-meridional transport circulation of the troposphere in an idealized {GCM}, J. Atmos. Sci., 59(9), 1502–1514, doi:10.1175/1520-0469(2002)059<1502:TMMTCO>2.0.CO;2, 2002.
Brewer, A. W.: Evidence for a world circulation provided by the measurements of helium and water vapour distribution in the stratosphere, Q. J. R. Meteorol. Soc., 75(326), 351–363, doi:10.1002/qj.49707532603, 1949.
Corti, T., Luo, B. P., de Reus, M., Brunner, D., Cairo, F., Mahoney, M. J., Martucci, G., Matthey, R., Mitev, V., dos Santos, F. H., Schiller, C., Shur, G., Sitnikov, N. M., Spelten, N., Vössing, H. J., Borrmann, S. and Peter, T.: Unprecedented evidence for deep convection hydrating the tropical stratosphere, Geophys. Res. Lett., 35(10), n/a--n/a, doi:10.1029/2008GL033641, 2008.
Dessler, A. E. and Sherwood, S. C.: Effect of convection on the summertime extratropical lower stratosphere, J. Geophys. Res. Atmos., 109(D23), doi:10.1029/2004JD005209, 2004.
Dessler, A. E., Hanisco, T. F. and Fueglistaler, S.: Effects of convective ice lofting on H 2 O and HDO in the tropical tropopause layer, J. Geophys. Res., 112(D18), D18309, doi:10.1029/2007JD008609, 2007.
Dessler, A. E., Ye, H., Wang, T., Schoeberl, M. R., Oman, L. D., Douglass, A. R., Butler, A. H., Rosenlof, K. H., Davis, S. M. and Portmann, R. W.: Transport of ice into the stratosphere and the humidification of the stratosphere over the 21st century, Geophys. Res. Lett., 43(5), 2323–2329, doi:10.1002/2016GL067991, 2016.
Dethof, A., O'Neill, A., Slingo, J. M. and Smit, H. G. J.: A mechanism for moistening the lower stratosphere involving the Asian summer monsoon, Q. J. R. Meteorol. Soc., 125(556), 1079–1106, doi:10.1002/qj.1999.49712555602, 1999.

Dvortsov, V. L. and Solomon, S.: Response of the stratospheric temperatures and ozone to past and future increases in stratospheric humidity, J. Geophys. Res. Atmos., 106(D7), 7505–7514, doi:10.1029/2000JD900637, 2001.

Fu, R., Hu, Y., Wright, J. S., Jiang, J. H., Dickinson, R. E., Chen, M., Filipiak, M., Read, W. G., Waters, J. W. and Wu, D. L.: Short circuit of water vapor and polluted air to the global stratosphere by convective transport over the Tibetan Plateau, , 103(15), 5664–5669, doi:10.1073/pnas.0601584103, 2006.

Fueglistaler, S.: Stratospheric water vapor predicted from the Lagrangian temperature history of air entering the stratosphere in the tropics, J. Geophys. Res., 110(D8), D08107, doi:10.1029/2004JD005516, 2005.

Fueglistaler, S., Dessler, A. E., Dunkerton, T. J., Folkins, I., Fu, Q. and Mote, P. W.: Tropical tropopause layer, Rev. Geophys., 47, 1–31, doi:10.1029/2008RG000267, 2009.

Gelaro, R., McCarty, W., Suárez, M. J., Todling, R., Molod, A., Takacs, L., Randles, C. A., Darmenov, A., Bosilovich, M. G., Reichle, R., Wargan, K., Coy, L., Cullather, R., Draper, C., Akella, S., Buchard, V., Conaty, A., da Silva, A. M., Gu, W., Kim, G.-K., Koster, R., Lucchesi, R., Merkova, D., Nielsen, J. E., Partyka, G., Pawson, S., Putman, W., Rienecker, M., Schubert, S. D., Sienkiewicz, M. and Zhao, B.: The Modern-Era Retrospective Analysis for Research and Applications, Version 2 (MERRA-2), J. Clim., 30(14), 5419–5454, doi:10.1175/JCLI-D-16-0758.1, 2017.

Gent, P. R., Danabasoglu, G., Donner, L. J., Holland, M. M., Hunke, E. C., Jayne, S. R., Lawrence, D. M., Neale, R. B., Rasch, P. J., Vertenstein, M., Worley, P. H., Yang, Z.-L. and Zhang, M.: The Community Climate System Model Version 4, J. Clim., 24(19), 4973–4991, doi:10.1175/2011JCLI4083.1, 2011.

Gettelman, A., Kinnison, D. E., Dunkerton, T. J. and Brasseur, G. P.: Impact of monsoon circulations on the upper troposphere and lower stratosphere, J. Geophys. Res. Atmos., 109(D22), doi:10.1029/2004JD004878, 2004.

Heymsfield, A., Winker, D., Avery, M., Vaughan, M., Diskin, G., Deng, M., Mitev, V. and Matthey, R.: Relationships between Ice Water Content and Volume Extinction Coefficient from In Situ Observations for Temperatures from 0° to −86°C: Implications for Spaceborne Lidar Retrievals*, J. Appl. Meteorol. Climatol., 53(2), 479–505, doi:10.1175/JAMC-D-13-087.1, 2014.

Holton, J. R., Haynes, P. H., McIntyre, M. E., Douglass, A. R., Rood, R. B. and Pfister, L.: Stratosphere-troposphere exchange, Rev. Geophys., 33(4), 403, doi:10.1029/95RG02097, 1995.

Hu, Y., Winker, D., Vaughan, M., Lin, B., Omar, A., Trepte, C., Flittner, D., Yang, P., Nasiri, S. L., Baum, B., Holz, R., Sun, W., Liu, Z., Wang, Z., Young, S., Stamnes, K., Huang, J. and Kuehn, R.: CALIPSO/CALIOP Cloud Phase Discrimination Algorithm, J. Atmos. Ocean. Technol., 26(11), 2293–2309, doi:10.1175/2009JTECHA1280.1, 2009.

Jackson, D. R., Driscoll, S. J., Highwood, E. J., Harries, J. E. and Russell, J. M.: Troposphere to stratosphere transport at low latitudes as studies using HALOE observations of water vapour 1992–1997, Q. J. R. Meteorol. Soc., 124(545), 169–192, doi:10.1002/qj.49712454508, 1998.

James, R., Bonazzola, M., Legras, B., Surbled, K. and Fueglistaler, S.: Water vapor transport and dehydration above convective outflow during Asian monsoon, Geophys. Res. Lett., 35(20), doi:10.1029/2008GL035441, 2008.

Kärcher, B., Hendricks, J. and Lohmann, U.: Physically based parameterization of cirrus cloud formation for use in global atmospheric models, J. Geophys. Res., 111(D1), D01205, doi:10.1029/2005JD006219, 2006.

Lambert, A., Read, W. G., Livesey, N. J., Santee, M. L., Manney, G. L., Froidevaux, L., Wu, D. L., Schwartz, M. J., Pumphrey, H. C., Jimenez, C., Nedoluha, G. E., Cofield, R. E., Cuddy, D. T., Daffer, W. H., Drouin, B. J., Fuller, R. A., Jarnot, R. F., Knosp, B. W., Pickett, H. M., Perun, V. S., Snyder, W. V, Stek, P. C., Thurstans, R. P., Wagner, P. A., Waters, J. W., Jucks, K. W., Toon, G. C., Stachnik, R. A., Bernath, P. F., Boone, C. D., Walker, K. A., Urban, J., Murtagh, D., Elkins, J. W. and Atlas, E.: Validation of the Aura Microwave Limb Sounder middle atmosphere water vapor and nitrous oxide measurements, J. Geophys. Res. Atmos., 112(D24), D24S36, doi:10.1029/2007JD008724, 2007.

Liu, Z., Vaughan, M., Winker, D., Kittaka, C., Getzewich, B., Kuehn, R., Omar, A., Powell, K., Trepte, C. and Hostetler, C.: The CALIPSO Lidar Cloud and Aerosol Discrimination: Version 2 Algorithm and Initial Assessment of Performance, J. Atmos. Ocean. Technol., 26(7), 1198–1213, doi:10.1175/2009JTECHA1229.1, 2009.

Livesey, N. J., Read, W. G., Wagner, P. A., Froidevaux, L., Lambert, A., Manney, G. L., Millán-Valle, L. F., Pumphrey, H. C., Santee, M. L., Schwartz, M. J., Wang, S., Fuller, R. A., Jarnot, R. F., Knosp, B. W., and Martinez, E.: Earth Observing System (EOS) Aura Microwave Limb Sounder (MLS), Version 4.2x Level 2 data quality and description document, Tech. Rep. JPL D-33509, Tech. Rep. version 4.2x-3.0, NASA Jet Propulsion Laboratory, 2017.

Luo, J., Pan, L. L., Honomichl, S. B., Bergman, J. W., Randel, W. J., Francis, G., Clerbaux, C., George, M., Liu, X. and

Atmos. Chem. Phys. Discuss., https://doi.org/10.5194/acp-2019-302
Manuscript under review for journal Atmos. Chem. Phys.
Discussion started: 29 April 2019

Tian, W.: Space–time variability in UTLS chemical distribution in the Asian summer monsoon viewed by limb and nadir satellite sensors, Atmos. Chem. Phys., 18(16), 12511–12530, doi:10.5194/acp-18-12511-2018, 2018.

Molod, A., Takacs, L., Suarez, M., Bacmeister, J., Song, I.-S., and Eichmann, A.: The GEOS-5 atmospheric general circulation model: Mean climate and development from MERRA to Fortuna, Technical Report Series on Global Modeling and Data Assimilation Volume 28, NASA Goddard Space Flight Center, 2012.

Molod, A., Takacs, L., Suarez, M. and Bacmeister, J.: Development of the GEOS-5 atmospheric general circulation model: evolution from MERRA to MERRA2, Geosci. Model Dev., 8(5), 1339–1356, doi:10.5194/gmd-8-1339-2015, 2015.

Moorthi, S. and Suarez, M. J.: Relaxed Arakawa-Schubert. A Parameterization of Moist Convection for General Circulation Models, Mon. Weather Rev., 120(6), 978–1002, doi:10.1175/1520-0493(1992)120<0978:RASAPO>2.0.CO;2, 1992.

Mote, P. W., Rosenloh, K. H., Holton, J. R., Harwood, R. S. and Waters, J. W.: Seasonal variations of water vapor in the tropical lower stratosphere, Geophys. Res. Lett., 22(9), 1093–1096, doi:10.1029/95GL01234, 1995.

Mote, P. W., Rosenlof, K. H., McIntyre, M. E., Carr, E. S., Gille, J. C., Holton, J. R., Kinnersley, J. S., Pumphrey, H. C., Russell III, J. M. and Waters, J. W.: An atmospheric tape recorder: The imprint of tropical tropopause temperatures on stratospheric water vapor, J. Geophys. Res., 101(D2), 3989–4006, doi:10.1029/95JD03422, 1996.

Moyer, E. J., Irion, F. W., Yung, Y. L. and Gunson, M. R.: ATMOS stratospheric deuterated water and implications for troposphere-stratosphere transport, Geophys. Res. Lett., 23(17), 2385–2388, doi:10.1029/96GL01489, 1996.

Murphy, D. M. and Koop, T.: Review of the vapour pressures of ice and supercooled water for atmospheric applications, Q. J. R. Meteorol. Soc., 131(608), 1539–1565, doi:10.1256/qj.04.94, 2005.

Nielsen, J. K., Larsen, N., Cairo, F., Donfrancesco, G. Di, Rosen, J. M., Durry, G., Held, G. and Pommereau, J.-P.: Solid particles in the tropical lowest stratosphere, Atmos. Chem. Phys., 7(3), 685–695, doi:10.5194/acp-7-685-2007, 2007.

Oman, L. D. and Douglass, A. R.: Improvements in total column ozone in GEOSCCM and comparisons with a new ozone-depleting substances scenario, J. Geophys. Res. Atmos., 119(9), 5613–5624, doi:10.1002/2014JD021590, 2014.

Pan, L., Solomon, S., Randel, W., Lamarque, J.-F., Hess, P., Gille, J., Chiou, E.-W. and McCormick, M. P.: Hemispheric asymmetries and seasonal variations of the lowermost stratospheric water vapor and ozone derived from SAGE II data, J. Geophys. Res. Atmos., 102(D23), 28177–28184, doi:10.1029/97JD02778, 1997.

Pan, L. L., Hintsa, E. J., Stone, E. M., Weinstock, E. M. and Randel, W. J.: The seasonal cycle of water vapor and saturation vapor mixing ratio in the extratropical lowermost stratosphere, J. Geophys. Res. Atmos., 105(D21), 26519–26530, doi:10.1029/2000JD900401, 2000.

Pan, L. L., Honomichl, S. B., Kinnison, D. E., Abalos, M., Randel, W. J., Bergman, J. W. and Bian, J.: Transport of chemical tracers from the boundary layer to stratosphere associated with the dynamics of the Asian summer monsoon, J. Geophys. Res. Atmos., 121(23), 14,159-14,174, doi:10.1002/2016JD025616, 2016.

Park, M., Randel, W. J., Kinnison, D. E., Garcia, R. R. and Choi, W.: Seasonal variation of methane, water vapor, and nitrogen oxides near the tropopause: Satellite observations and model simulations, J. Geophys. Res. Atmos., 109(D3), n/a-n/a, doi:10.1029/2003JD003706, 2004.

Park, M., Randel, W. J., Gettelman, A., Massie, S. T. and Jiang, J. H.: Transport above the Asian summer monsoon anticyclone inferred from Aura Microwave Limb Sounder tracers, J. Geophys. Res. Atmos., 112(D16), 2007.

Pawson, S., Stolarski, R. S., Douglass, A. R., Newman, P. A., Nielsen, J. E., Frith, S. M. and Gupta, M. L.: Goddard Earth Observing System chemistry-climate model simulations of stratospheric ozone-temperature coupling between 1950 and 2005, J. Geophys. Res., 113(D12), D12103, doi:10.1029/2007JD009511, 2008.

Ploeger, F., Günther, G., Konopka, P., Fueglistaler, S., Müller, R., Hoppe, C., Kunz, A., Spang, R., Grooß, J.-U. and Riese, M.: Horizontal water vapor transport in the lower stratosphere from subtropics to high latitudes during boreal summer, J. Geophys. Res. Atmos., 118(14), 8111–8127, doi:10.1002/jgrd.50636, 2013.

Randel, W. J. and Park, M.: Deep convective influence on the Asian summer monsoon anticyclone and associated tracer variability observed with Atmospheric Infrared Sounder (AIRS), J. Geophys. Res., 111(D12), D12314, doi:10.1029/2005JD006490, 2006.

Randel, W. J., Wu, F., Russell, J. M., Roche, A. and Waters, J. W.: Seasonal Cycles and QBO Variations in Stratospheric CH4and H2O Observed inUARSHALOE Data, J. Atmos. Sci., 55(2), 163–185, doi:10.1175/1520-0469(1998)055<0163:Scaqvi>2.0.Co;2, 1998.

Randel, W. J., Wu, F., Gettelman, A., Russell, J. M., Zawodny, J. M. and Oltmans, S. J.: Seasonal variation of water vapor in the lower stratosphere observed in Halogen Occultation Experiment data, J. Geophys. Res. Atmos., 106(D13), 14313–

14325, doi:10.1029/2001jd900048, 2001.
Randel, W. J., Zhang, K. and Fu, R.: What controls stratospheric water vapor in the NH summer monsoon regions?, J. Geophys. Res. Atmos., 120(15), 7988–8001, doi:10.1002/2015JD023622, 2015.
Rienecker, M.M., Suarez, M.J., Todling, R., Bacmeister, J., Takacs, L., Liu, H.-C., Gu, W., Sienkiewicz, M., Koster, R.D., Gelaro, R., Stajner, I., and Nielsen J.E.: The GEOS-5 data assimilation system—Documentation of versions 5.0.1, 5.1.0, and 5.2.0, Technical Report Series on Global Modeling and Data Assimilation, Volume 27, NASA Goddard Space Flight Center Greenbelt, 2008.
Rosenlof, K. H.: Hemispheric asymmetries in water vapor and inferences about transport in the lower stratosphere, J. Geophys. Res. Atmos., 102(D11), 13213–13234, doi:10.1029/97JD00873, 1997.
Schoeberl, M. R. and Dessler, A. E.: Dehydration of the stratosphere, Atmos. Chem. Phys., 11(16), 8433–8446, doi:10.5194/acp-11-8433-2011, 2011.
Schoeberl, M. R., Douglass, A. R., Newman, P. A., Lait, L. R., Lary, D., Waters, J., Livesey, N., Froidevaux, L., Lambert, A., Read, W., Filipiak, M. J. and Pumphrey, H. C.: QBO and annual cycle variations in tropical lower stratosphere trace gases from HALOE and Aura MLS observations, J. Geophys. Res. Atmos., 113(D5), n/a-n/a, doi:10.1029/2007JD008678, 2008.
Schoeberl, M. R., Dessler, A. E., Wang, T., Avery, M. A. and Jensen, E. J.: Cloud formation, convection, and stratospheric dehydration, Earth Sp. Sci., 1(1), 1–17, doi:10.1002/2014EA000014, 2014.
Schoeberl, M. R., Jensen, E. J. and Woods, S.: Gravity waves amplify upper tropospheric dehydration by clouds, Earth Sp. Sci., 2(12), 485–500, doi:10.1002/2015EA000127, 2015.
Schoeberl, M. R., Jensen, E. J., Pfister, L., Ueyama, R., Avery, M. and Dessler, A. E.: Convective Hydration of the Upper Troposphere and Lower Stratosphere, J. Geophys. Res. Atmos., 123(9), 4583–4593, doi:10.1029/2018JD028286, 2018.
Schwartz, M. J., Read, W. G., Santee, M. L., Livesey, N. J., Froidevaux, L., Lambert, A. and Manney, G. L.: Convectively injected water vapor in the North American summer lowermost stratosphere, Geophys. Res. Lett., 40(10), 2316–2321, doi:10.1002/grl.50421, 2013.
Solomon, S., Garcia, R. R., Rowland, F. S. and Wuebbles, D. J.: On the depletion of Antarctic ozone, Nature, 321(6072), 755–758, doi:doi:10.1038/321755a0, 1986.
Steinwagner, J., Fueglistaler, S., Stiller, G., von Clarmann, T., Kiefer, M., Borsboom, P.-P., van Delden, A. and Röckmann, T.: Tropical dehydration processes constrained by the seasonality of stratospheric deuterated water, Nat. Geosci., 3, 262, doi:10.1038/ngeo822, 2010.
Ueyama, R., Jensen, E. J., Pfister, L. and Kim, J.-E.: Dynamical, convective, and microphysical control on wintertime distributions of water vapor and clouds in the tropical tropopause layer, J. Geophys. Res. Atmos., 120(19), 10,410-483,500, doi:10.1002/2015JD023318, 2015.
Vaughan, M. A., Powell, K. A., Winker, D. M., Hostetler, C. A., Kuehn, R. E., Hunt, W. H., Getzewich, B. J., Young, S. A., Liu, Z. and McGill, M. J.: Fully Automated Detection of Cloud and Aerosol Layers in the CALIPSO Lidar Measurements, J. Atmos. Ocean. Technol., 26(10), 2034–2050, doi:10.1175/2009JTECHA1228.1, 2009.
Van Vuuren, D. P., Edmonds, J., Kainuma, M., Riahi, K., Thomson, A., Hibbard, K., Hurtt, G. C., Kram, T., Krey, V., Lamarque, J.-F. and others: The representative concentration pathways: an overview, Clim. Change, 109, 5–31, doi:10.1007/s10584-011-0148-z, 2011.
Winker, D. M., Vaughan, M. A., Omar, A., Hu, Y., Powell, K. A., Liu, Z., Hunt, W. H. and Young, S. A.: Overview of the CALIPSO Mission and CALIOP Data Processing Algorithms, J. Atmos. Ocean. Technol., 26(11), 2310–2323, doi:10.1175/2009jtecha1281.1, 2009.
Winker, D. M., Pelon, J., Coakley, J. A., Ackerman, S. A., Charlson, R. J., Colarco, P. R., Flamant, P., Fu, Q., Hoff, R. M., Kittaka, C., Kubar, T. L., Le Treut, H., Mccormick, M. P., Mégie, G., Poole, L., Powell, K., Trepte, C., Vaughan, M. A. and Wielicki, B. A.: The CALIPSO Mission, Bull. Am. Meteorol. Soc., 91(9), 1211–1230, doi:10.1175/2010BAMS3009.1, 2010.
Woods, S., Lawson, R. P., Jensen, E., Bui, T. P., Thornberry, T., Rollins, A., Pfister, L. and Avery, M.: Microphysical Properties of Tropical Tropopause Layer Cirrus, J. Geophys. Res. Atmos., 123(11), 6053–6069, doi:10.1029/2017JD028068, 2018.
World Meteorological Organization: Scientific assessment of ozone depletion, Global Ozone Research and Monitoring Project–Report No. 52, Geneva, Switzerland, 2010.

Wright, J. S., Fu, R., Fueglistaler, S., Liu, Y. S. and Zhang, Y.: The influence of summertime convection over Southeast Asia on water vapor in the tropical stratosphere, J. Geophys. Res. Atmos., 116(D12), 1–12, doi:10.1029/2010JD015416, 2011.

Ye, H., Dessler, A. E. and Yu, W.: Effects of convective ice evaporation on interannual variability of tropical tropopause layer water vapor, Atmos. Chem. Phys., 18(7), 4425–4437, doi:10.5194/acp-18-4425-2018, 2018.

Young, S. A. and Vaughan, M. A.: The Retrieval of Profiles of Particulate Extinction from Cloud-Aerosol Lidar Infrared Pathfinder Satellite Observations (CALIPSO) Data: Algorithm Description, J. Atmos. Ocean. Technol., 26(6), 1105–1119, doi:10.1175/2008JTECHA1221.1, 2009.

Atmos. Chem. Phys. Discuss., https://doi.org/10.5194/acp-2019-302
Manuscript under review for journal Atmos. Chem. Phys.
Discussion started: 29 April 2019

Table 1: Summary of trajectory model cases

Trajectory Model Cases	Description
ERAi standard trajectory model	Instant dehydration with no convective influence
MERRA-2 standard trajectory model	Instant dehydration with no convective influence
ERAi trajectory with cloud model	Dehydration with the cloud model, but with no convective influence
MERRA-2 trajectory with cloud model	Dehydration with the cloud model, but with no convective influence
GEOSCCM standard trajectory model	Instant dehydration with no convective influence
GEOSCCM ice model	Instant dehydration. Convective ice instantly evaporates to sub-saturated parcels
GEOSCCM ice model+ τ	Instant dehydration. Convective ice evaporates to sub-saturated parcels and relaxes the RH towards pre-set threshold with an e-folding time scale τ

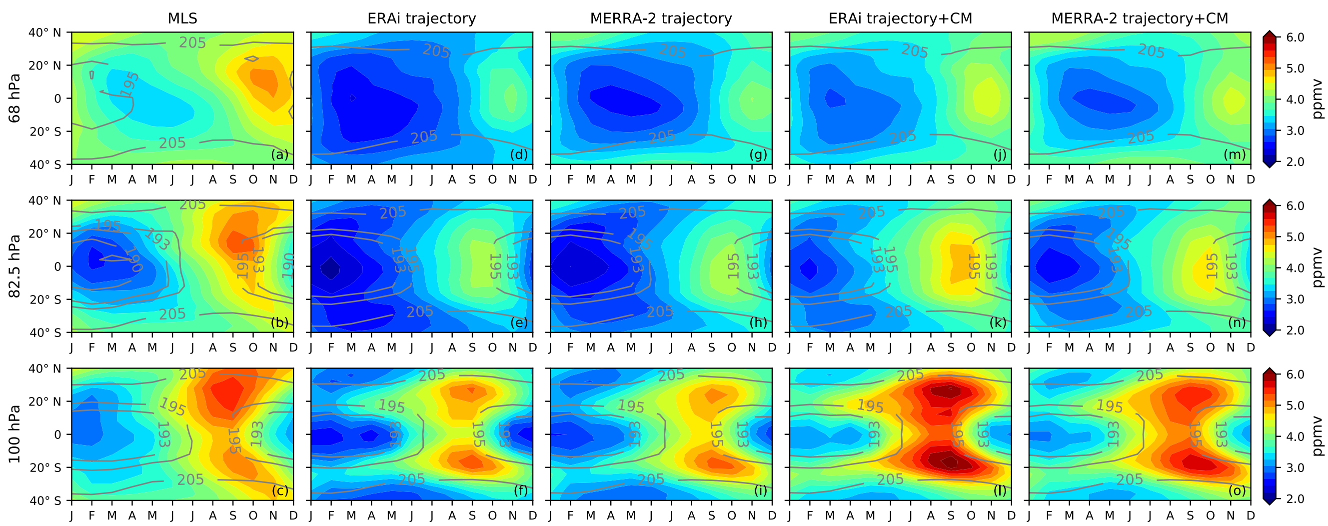

Figure 1: Zonal mean seasonal cycle water vapor (ppmv, color shading) and temperature (K, contour lines) between 40°S - 40°N from (a)-(c) MLS, (d)-(f) ERAi trajectory model, (g)-(i) MERRA-2 trajectory model, (j)-(l) ERAi trajectory model with the cloud model, and (m)-(o) MERRA-2 trajectory model with the cloud model at 68 hPa (top row), 82.5 hPa (middle row) and 100 hPa (bottom row).

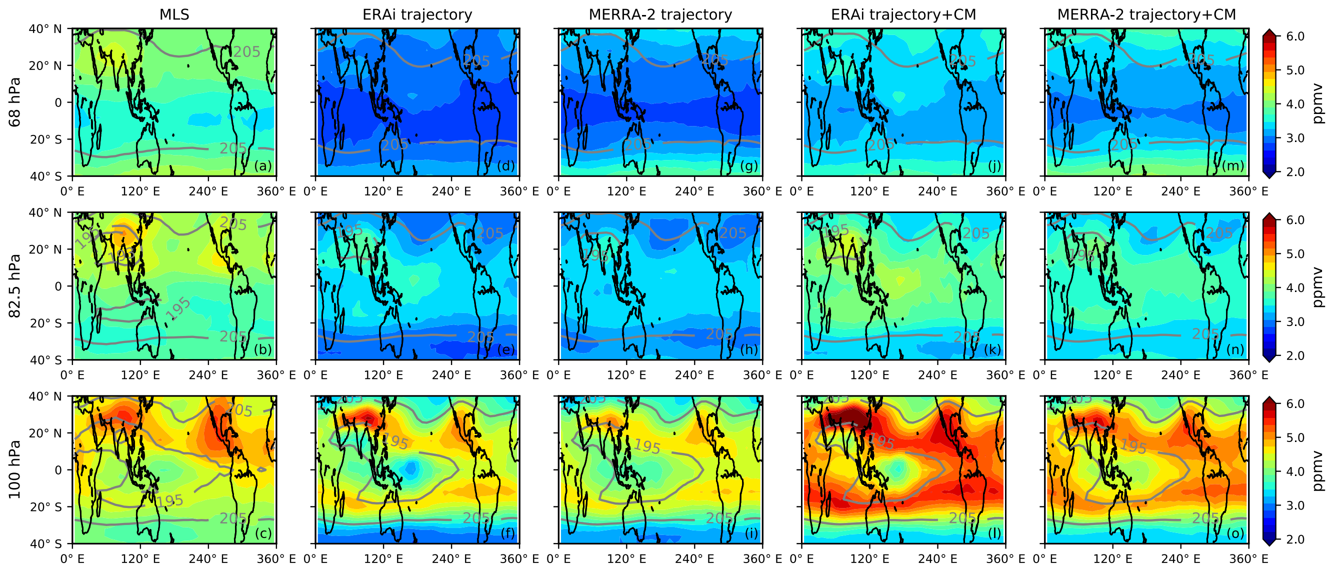

Figure 2: JJA water vapor (ppmv, color shading) and temperature (K, contour lines) between 40°S - 40°N from (a)-(c) MLS, (d)-(f) ERAi trajectory model, (g)-(i) MERRA-2 trajectory model, (j)-(l) ERAi trajectory model with the cloud model, and (m)-(o) MERRA-2 trajectory model with the cloud model at 68 hPa (top row), 82.5 hPa (middle row) and 100 hPa (bottom row).

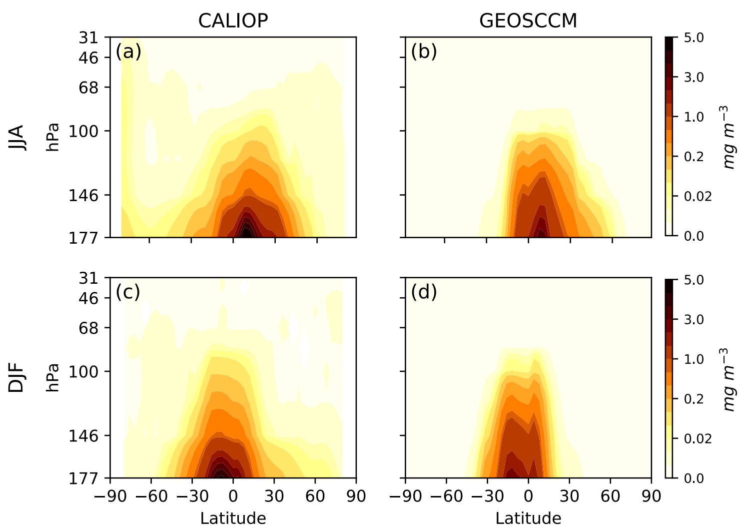

Figure 3. 2007-2017 Zonal mean IWC (mg m^{-3}) from (left) CALIOP and (right) GEOSCCM for June-July-August (JJA, top row), and for December-January-February (DJF, bottom row). Note we use a nonlinear color scale.

Atmos. Chem. Phys. Discuss., https://doi.org/10.5194/acp-2019-302
Manuscript under review for journal Atmos. Chem. Phys.
Discussion started: 29 April 2019

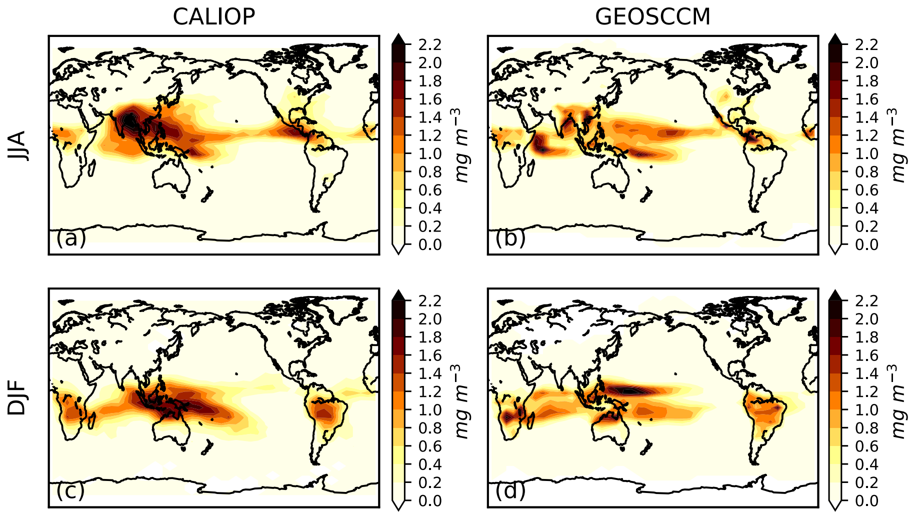

557
558 **Figure 4. 2007-2017 IWC (mg m^{-3}) from (left) CALIOP and (right) GEOSCCM averaged between 177-68 hPa for June-July-**
559 **August (JJA, top row), and for December-January-February (DJF, bottom row).**

Atmos. Chem. Phys. Discuss., https://doi.org/10.5194/acp-2019-302
Manuscript under review for journal Atmos. Chem. Phys.
Discussion started: 29 April 2019

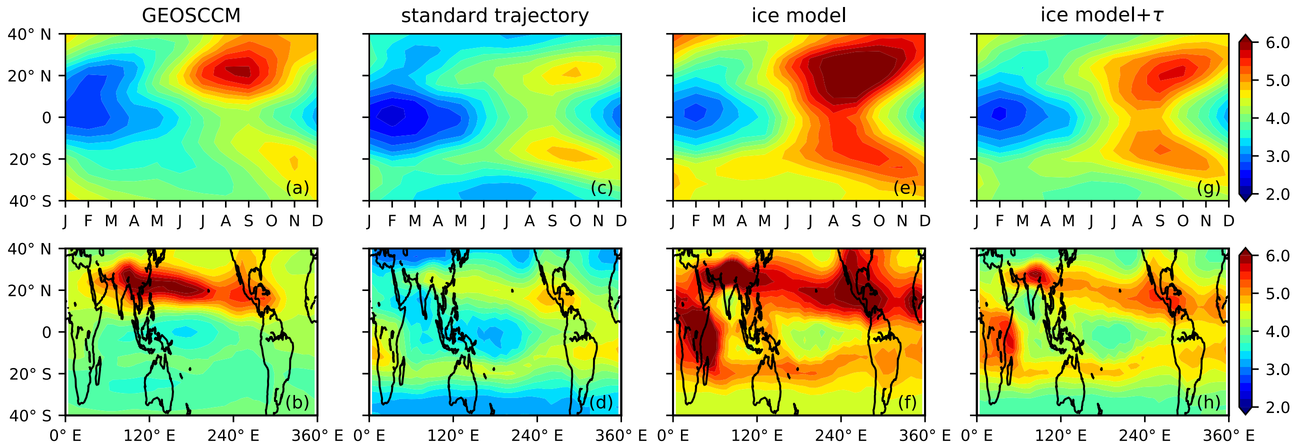

Figure 5. Top panel: Zonal mean seasonal cycle of 100-hPa water vapor (ppmv) between 40°S - 40°N from (a) GEOSCCM, (c) standard model, (e) ice model, and (g) ice model with a finite time ice evaporation scheme. Bottom panel: JJA 100-hPa water vapor (ppmv) between 40°S - 40°N from (b) GEOSCCM, (d) standard model, (f) ice model, and (h) ice model with a finite time ice evaporation scheme.

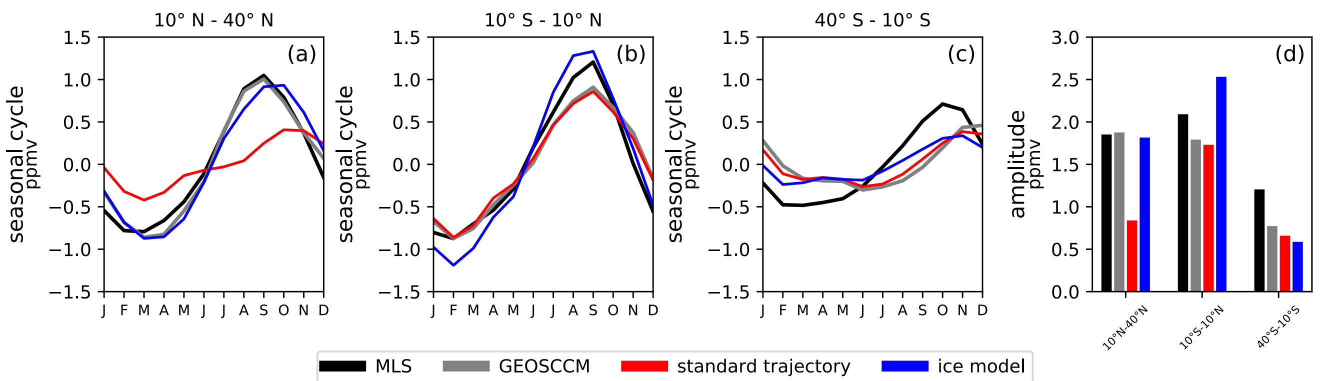

Figure 6. Seasonal cycles of water vapor at 100 hPa averaged between (a) 10°N-40°N, (b) 10°S-10°N, and (c) 40°S-10°S and their (d) seasonal amplitudes from GEOSCCM, standard model, and ice model. We have subtracted the annual mean from each data set.

Atmos. Chem. Phys. Discuss., https://doi.org/10.5194/acp-2019-302
Manuscript under review for journal Atmos. Chem. Phys.
Discussion started: 29 April 2019

Atmospheric Chemistry and Physics
Discussions

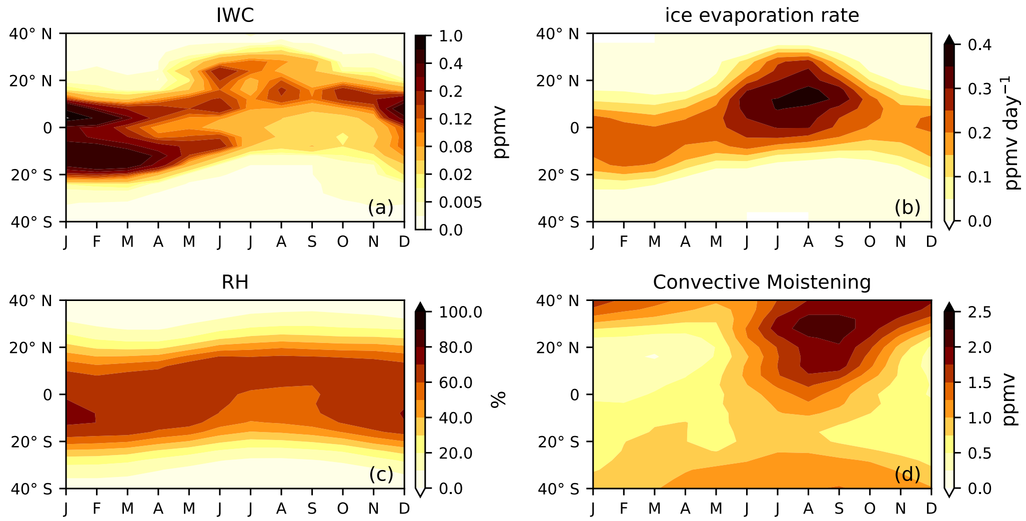

Figure 7. (a) Zonal mean seasonal cycle of 100-hPa convective lofted IWC (ppmv) from GEOSCCM. Note the color scale is nonlinear. (b) Zonal mean seasonal cycle of 100-hPa evaporation rate (ppmv day-1) from the ice model. (c) Zonal mean seasonal cycle of relative humidity (%) with respect to ice at 100 hPa from GEOSCCM. (d) Zonal mean seasonal cycle of net convective moistening (ppmv) at 100 hPa from the ice model. The quantity net convective moistening is the difference between water vapor values from the ice model and standard model.

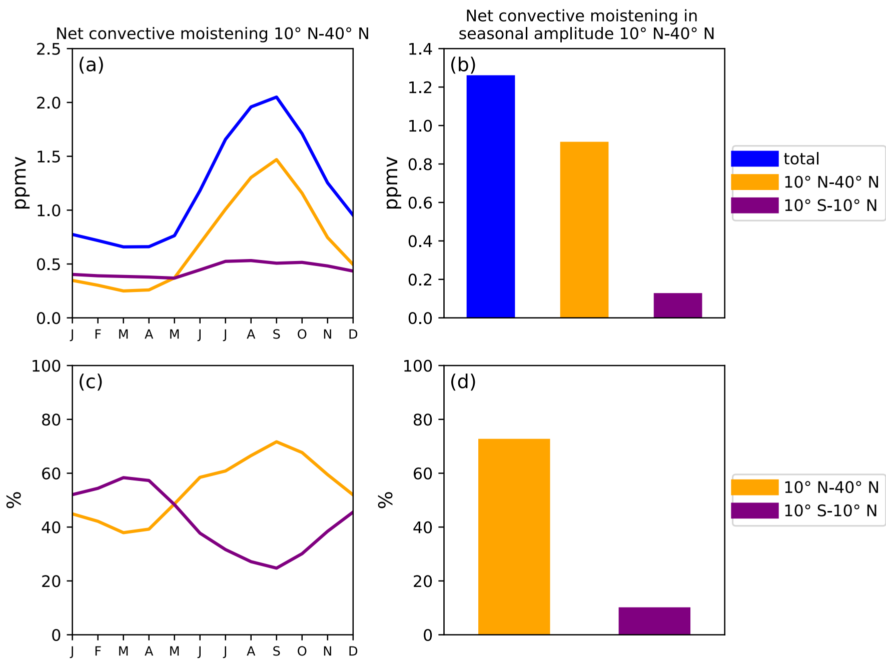

Figure 8. (a) Net convective moistening (ppmv) in the 10°N-40°N water vapor seasonal cycle and the portions (ppmv) contributed by convective ice evaporation over 10°S-10°N and 10°N-40°N. (b) Net convective moistening (ppmv) in the 10°N-40°N water vapor seasonal amplitude and the portions (ppmv) contributed by convective ice evaporation over 10°S-10°N and 10°N-40°N. (c)-(d) Percentage of net convective moistening in the 10°N-40°N water vapor seasonal cycle and seasonal amplitude contributed by convective ice evaporation over 10°S-10°N and 10°N-40°N. The percentage is net convective moistening contributed by 10°S-10°N or 10°N-40°N region divided by the total net convective moistening.

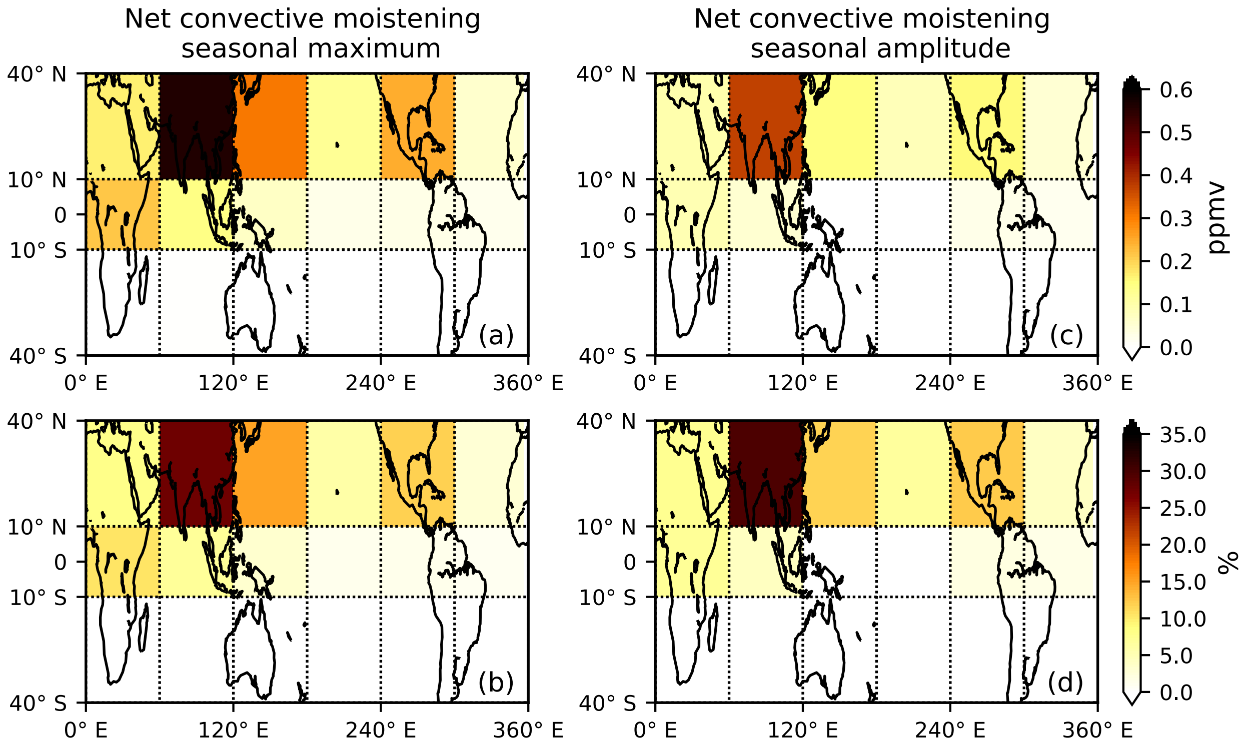

583
584 **Figure 9. Portions of net convective moistening (ppmv) in the (a) maximum value and (b) seasonal amplitude of the 10°N-40°N**
585 **water vapor seasonal cycle contributed by 12 equal-area box regions between 10°S-40°N. (c) and (d): Same as (a) and (b), but for**
586 **the percentage of net convective moistening contributed by the 12 equal-area box regions.**